Journal of Applied Electrochemistry (2023) 53:781–795
https://doi.org/10.1007/s10800-022-01806-7

RESEARCH ARTICLE

Precursor solution concentration-dependent electrochemical supercapacitive behavior of spray-deposited RuO_2 films using aqueous/organic solvent mixtures

Chandrashekhar R. Chikkegowda[1] · Abhijit A. Yadav[1]

Received: 5 October 2022 / Accepted: 10 November 2022 / Published online: 12 December 2022
© The Author(s), under exclusive licence to Springer Nature B.V. 2022

Abstract

RuO_2 electrodes are spray-deposited with various precursor solution concentrations using aqueous/organic solvent mixtures. RuO_2 has a preferential growth along the (110) plane of the rutile tetragonal crystal structure with porous morphology. The bandgap decreases from 2.05 to 1.77 eV with increasing precursor solution concentrations. Electrical resistivity of 0.12×10^4 Ωcm has been observed for RuO_2 films prepared with a 50 mM precursor solution concentration. RuO_2 film showed a specific capacitance of 893 Fg^{-1} at a scan rate of 5 mVs^{-1} and 964 Fg^{-1} at 0.5 Ag^{-1} with 93.67% capacitance retention over 1000 cycles. As a RuO_2 electrode supercapacitor device, the energy density reaches 76.56 $Whkg^{-1}$ at a power density of 1701 Wkg^{-1}. The solution resistance is about 0.32 Ω for the RuO_2 electrode prepared with a precursor solution concentration of 50 mM. The use of an aqueous/organic mixture as solvent improves the electrochemical supercapacitive performance of RuO_2 electrodes.

Graphical abstract

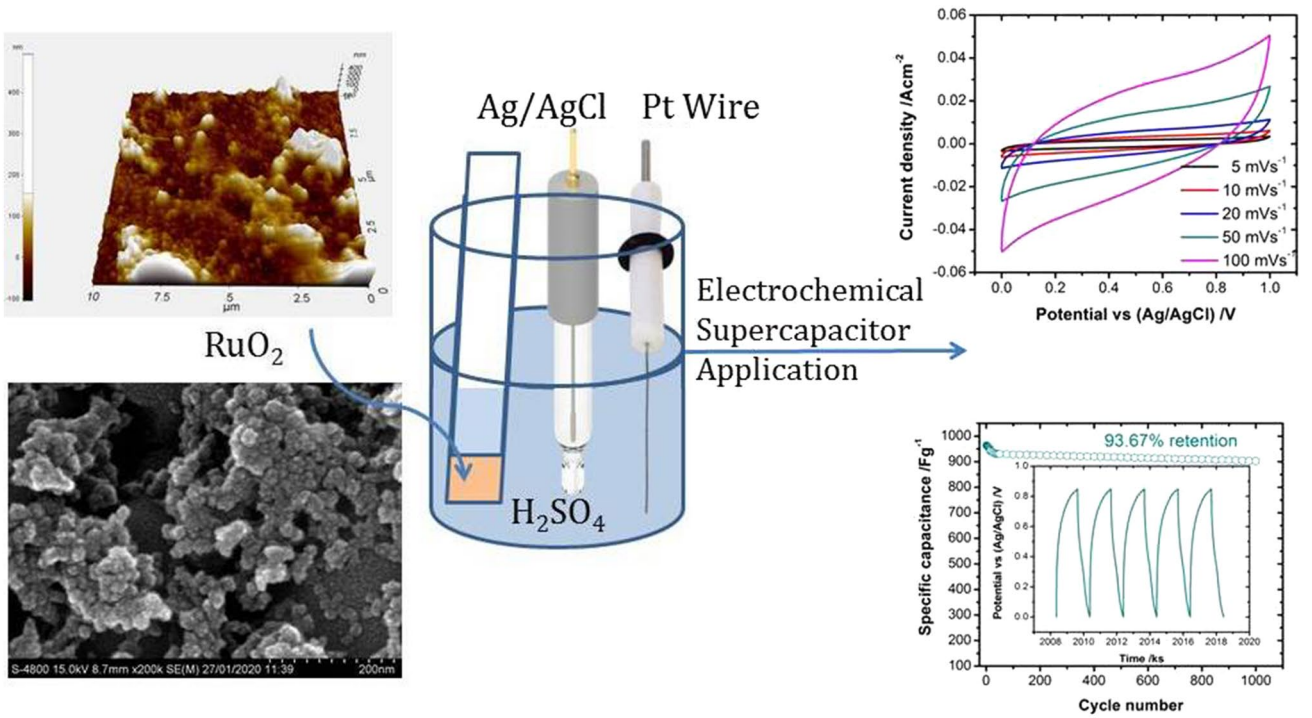

Extended author information available on the last page of the article

Keywords Spray pyrolysis · RuO_2 · Precursor solution concentration · Aqueous/organic solvent mixture · Supercapacitor

1 Introduction

The need for energy on a global scale is continuously rising because of economic and scientific growth. However, the fossil fuel supplies on Earth are running out. In addition, using fossil fuels will pollute the environment through the greenhouse effect and other means. As a result, all nations are making investments in sustainable and renewable energy sources [1]. To meet the problems of rising energy demand and the recurrent nature of renewable sources, like solar and wind, there is an increased need for sustainable energy storage technology [2]. Supercapacitors and other electrochemical capacitors are gaining popularity as cutting-edge energy storage technologies and are frequently utilized in portable electronic equipment, automobile systems, backup power systems, hybrid power cars, laptops, mobile phones, digital cameras, and other applications [3–5].

Pseudo-supercapacitors and electric double-layer capacitors (EDLCs) are two categories of supercapacitors based on different energy storage mechanisms. The capacitance of pseudo-supercapacitors result from rapid and reversible intercalation or redox reactions of electroactive species on the electrode surface, such as conducting polymers or transition metal oxides/hydroxides [1, 6]. At the interface between the electrode and the electrolyte, charge builds up through electrostatic interactions to store energy in the EDLC. Consequently, the accessible surface of the electrode material has a significant influence on the capacity of EDLCs. Since no chemical reaction occurs during the charge–discharge process, EDLCs have a lower capacity than pseudo-supercapacitors but a higher energy density and better cycling stability [7].

Two identical electrodes immersed in an electrolyte and a separator form a supercapacitor. To achieve excellent supercapacitive characteristics, there must be effective contact between the electrode and the electrolyte [8]. In supercapacitors, the quality of the electrode material is critical. Three different categories of electrode materials exist: conducting polymers, transition metal oxides/hydroxides, and carbon-based compounds. Carbon based electrodes have good electrical conductivity and chemical stability but a low specific capacity [9]. Conducting polymers exhibit high specific capacitance but have limited cycle life [10]. Compared to conducting polymers and carbon-based electrodes, metal oxides typically have multiple oxidation states that favor faster redox reactions, resulting in higher specific capacitance [11]. Among the transition metal oxides considered as supercapacitor electrode materials are ruthenium dioxide (RuO_2), manganese oxide (MnO_2 and Mn_3O_4), nickel oxide (NiO), molybdenum oxide (MoO_3), cobalt oxide (Co_3O_4), nickel cobaltite ($NiCo_2O_4$), iron oxide (Fe_2O_3), vanadium (V) oxide (V_2O_5), etc. [12–23].

RuO_2 has a quasi-rectangular cyclic voltammogram and a faradaic charge-transfer process. RuO_2's large surface area, fast proton transport, and good electrical conductivity all help produce a fast, reversible faradaic reaction with a high specific capacitance [12, 24, 25]. Majumdar et al. [26] have reviewed the progress of RuO_2 in terms of fabrication, design, and electrochemical performance. Patake et al. [27] deposited amorphous and porous RuO_2 films using electrodeposition and obtained a specific capacitance of 650 Fg^{-1} in 0.5 M H_2SO_4 electrolyte. Warren et al. [28] studied RuO_2 deposited by atomic layer deposition and measured a specific capacity of 644 Fg^{-1} with a high power density at 17 $kWkg^{-1}$. Park et al. [29] prepared RuO_2 electrodes by cathodic electrodeposition and studied the effect of film thickness on the electrochemical properties. A specific capacitance of 788 Fg^{-1} is obtained with an electrode thickness of 0.0014 gcm^{-2}. Zhang et al. [30] prepared nanotubular RuO_2 using template synthesis. A specific capacitance of 860 Fg^{-1} has been obtained at 500 mAg^{-1} in H_2SO_4 electrolyte.

Several methods have been used to deposit RuO_2 thin films, including sputtering [31], atomic layer deposition [32], electrode deposition [27, 29], template synthesis [30], SILAR [32], chemical bath deposition [33], spray pyrolysis [34–36], etc. Among these methods, spray pyrolysis is used to deposit thin films of noble metals, metal oxides, spinel oxides, and superconducting compounds without vacuum, and is simple and effective on both small and large-scale substrates. Therefore, a spray pyrolysis method was used to deposit RuO_2 films. The aim of the present work is to show how the electrochemical supercapacitive behavior of spray-deposited RuO_2 films can be improved by changing precursor solution concentrations in the aqueous/organic solvent mixture.

2 Experimental

To deposit RuO_2 films using spray pyrolysis, ruthenium(III) chloride trihydrate ($RuCl_3{\cdot}3H_2O$) was used as a precursor at an optimized substrate temperature of 290 °C. Required amounts of ruthenium(III) chloride trihydrate were dissolved in double distilled water to prepare precursor solution concentrations of 12.5 mM, 25 mM, 37.5 mM, 50 mM, and

62.5 mM. For each deposition, 20 ml of final spray solution was prepared by mixing 10 ml of this precursor solution with 10 ml of ethanol. The precursor solution was sprayed through a specially designed glass nozzle at a spray rate of 3–4 $mlmin^{-1}$ onto preheated ultrasonically cleaned amorphous glass and fluorine doped tin oxide (FTO) substrates, using air as the carrier gas at a pressure of 176 kPa. The distance between the glass nozzle and the substrate was kept approximately 28 cm.

The structural properties of the spray-deposited RuO_2 films were investigated with Cu-Kα radiation (wavelength $\lambda = 1.5406$ Å) using an X-ray diffractometer (Ultima IV, Rigaku Corporation, Japan). Surface morphologies of RuO_2 films deposited with various precursor solution concentrations were investigated by Field Emission Scanning Electron Microscope (FESEM), S-4800 Hitachi, Japan and Atomic force microscopy (AFM) (Digital Instruments Nanoscope III). Optical absorption spectra of RuO_2 films were captured using UV–Vis spectrophotometer (Ocean Optics JAZ-3 and NIR-QUEST) to estimate the optical band gap. Electrical resistivity was measured using the DC two-point probe technique. Electrochemical measurements of the RuO_2 films were carried out using an electrochemical analyzer (CHI 608D). A typical three-electrode cell arrangement was adopted with 1 cm^2 RuO_2 as a working electrode and platinum and saturated Ag/AgCl in 0.5 M H_2SO_4 electrolyte as the counter and reference electrodes. Galvanostatic charge–discharge (GCD), Cyclic voltammetry (CV), and electrochemical impedance spectroscopy (EIS) were among the electrochemical measures.

3 Results and discussion

When an aqueous/organic solvent mixture of ruthenium (III) chloride trihydrate in ethanol is sprayed onto amorphous glass and FTO coated glass substrates, fine droplets of the aqueous/organic mixture thermally decompose after falling on the surface of the heated substrate. Because the spray solution's reaction and decomposition processes on the substrate surface differ for each of the used solvents, the resulting film has distinct growth kinetics [27, 36]. A ruthenium (III) chloride trihydrate ($RuCl_3{\cdot}3H_2O$) in an aqueous/organic solvent mixture sprayed onto hot substrates supplies Ru^{3+} ions, a chemical reaction among Ru^{3+} and OH^- forms $Ru(OH)_3$, which decomposes to well-adherent RuO_2. The adherent dark black RuO_2 thin films are formed at the temperature of deposition. At an optimized substrate temperature, reactions can be,

$$2Ru(III)Cl_3 \cdot 3H_2O \rightarrow 2Ru^{3+} + 6OH^- + 6HCl \quad (1)$$

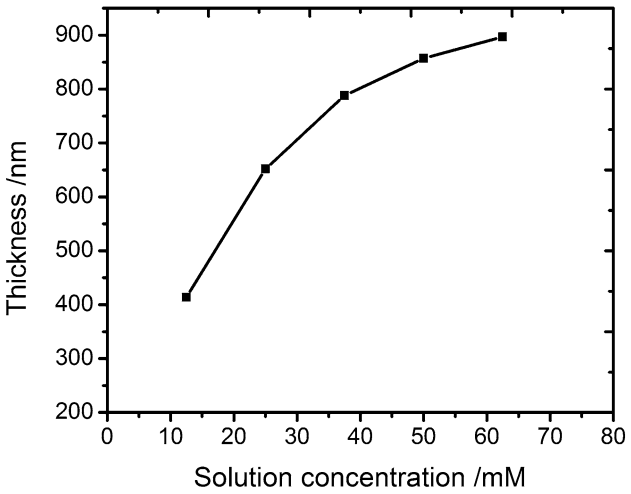

Fig. 1 Variation film thickness with precursor solution concentration for spray-deposited RuO_2 films

$$3OH^- + Ru^{3+} \rightarrow Ru(OH)_3 \quad (2)$$

$$OH^- + Ru(OH)_3 \rightarrow RuO_2 + 2H_2O \uparrow \quad (3)$$

Gujar et al. [36] have previously reported a similar reaction for RuO_2 films.

3.1 Film thickness

The spray-deposited RuO_2 electrodes with precursor solution concentrations of 12.5 mM, 25 mM, 37.5 mM, 50 mM, and 62.5 mM have resultant mass-loadings of 0.29, 0.45, 0.55, 0.60, and 0.63 $mgcm^{-2}$ respectively. The film thickness was

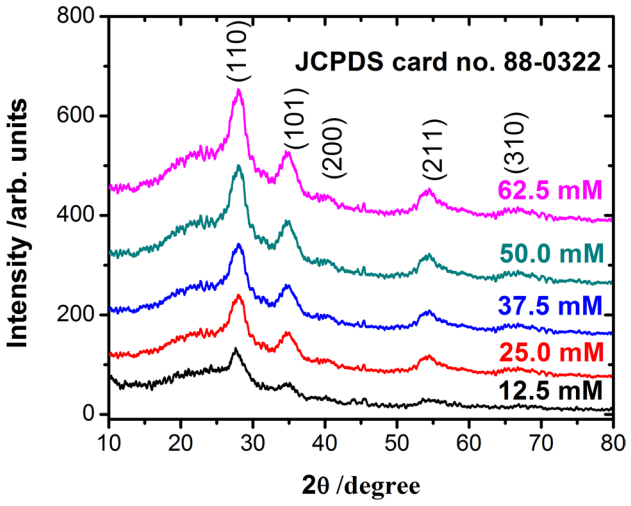

Fig. 2 XRD patterns of RuO_2 films spray-deposited with various precursor solution concentrations

Table 1 Structural data for RuO_2 films spray-deposited with various precursor solution concentrations

Solution Conc. (mM)	2θ (°)	d (Å) (Cal.)	d (Å) (Std.)	hkl	a (Å)	c (Å)	D (nm)
12.5	27.24	3.271	3.177	110	4.565	3.108	25
	34.89	2.569	2.555	101			
	40.00	2.252	2.247	200			
	53.89	1.700	1.687	211			
	66.40	1.407	1.421	310			
25	27.82	3.204	3.177	110	4.517	3.168	16
	34.55	2.594	2.555	101			
	40.00	2.252	2.247	200			
	54.20	1.691	1.687	211			
	66.43	1.406	1.421	310			
37.5	27.71	3.216	3.177	110	4.518	3.153	14
	34.66	2.586	2.555	101			
	40.16	2.243	2.247	200			
	54.00	1.697	1.687	211			
	66.48	1.405	1.421	310			
50	27.98	3.186	3.177	110	4.500	3.175	13
	34.54	2.594	2.555	101			
	40.08	2.248	2.247	200			
	54.24	1.690	1.687	211			
	65.96	1.415	1.421	310			
62.5	27.84	3.202	3.177	110	4.510	3.157	12
	34.65	2.586	2.555	101			
	40.10	2.247	2.247	200			
	54.17	1.692	1.687	211			
	65.52	1.423	1.421	310			

2θ Bragg's angle, *d* interplanar spacing, *hkl* Miller indices, '*a*' and '*c*' lattice constants, *D* crystallite size

measured using the gravimetric weight difference method [37] with a sensitive microbalance considering the bulk density of RuO_2 ($\rho = 6.97$ g/cm^3). For spray-deposited RuO_2 films, Fig. 1 depicts the variation of film thickness against precursor solution concentration. According to the graph, the film thickness increases gradually for each concentration as the precursor solution concentration increases up to 50 mM before saturation. It is clear that as the precursor solution concentration increases up to 50 mM, more precursor material contributes to the formation of the RuO_2 film, which also increases its thickness. The formation of tensile tensions, which have a propensity to disintegrate and make the film bulky, can be credited for the saturation of RuO_2 film thickness. Further, it can be seen that for a fixed amount of precursor solution (20 ml), the growth rate increased as the precursor solution's concentration increased, resulting in thicker RuO_2 films. The growth rate, however, was not proportional to the concentration of the precursor solution. Dhole and colleagues [38] observed similar film thickness behavior for electroplated NiO electrodes.

3.2 X-ray diffraction (XRD)

XRD patterns of RuO_2 films spray-deposited with various precursor solution concentrations are shown in Fig. 2. Spray-deposited RuO_2 films are polycrystalline. The obtained interplanar spacing values match the standard values, indicating that the spray-deposited films are composed of RuO_2 with rutile tetragonal crystal structure and space group P42 [39]. The diffraction peaks observed at 28.06°, 35.09°, 40.10°, 54.33°, and 65.65° can be attributed to the (110), (101), (200), (211), and (310) planes of RuO_2, respectively [JCPDS 88-0322]. As the precursor solution concentration increases to 50 mM, the film crystallinity increases and then begins to saturate. The increase in (110) peak intensity with increasing precursor solution concentration is either due to a continuous increase in film thickness from 414 to 897 nm, or an increase in the degree of crystallinity with increasing precursor solution concentration, or both [40]. Spray-deposited RuO_2 films show an orientation along the (110) plane, regardless of the precursor solution concentration used for deposition. Kim et al. [41] observed similar XRD patterns for electrospun

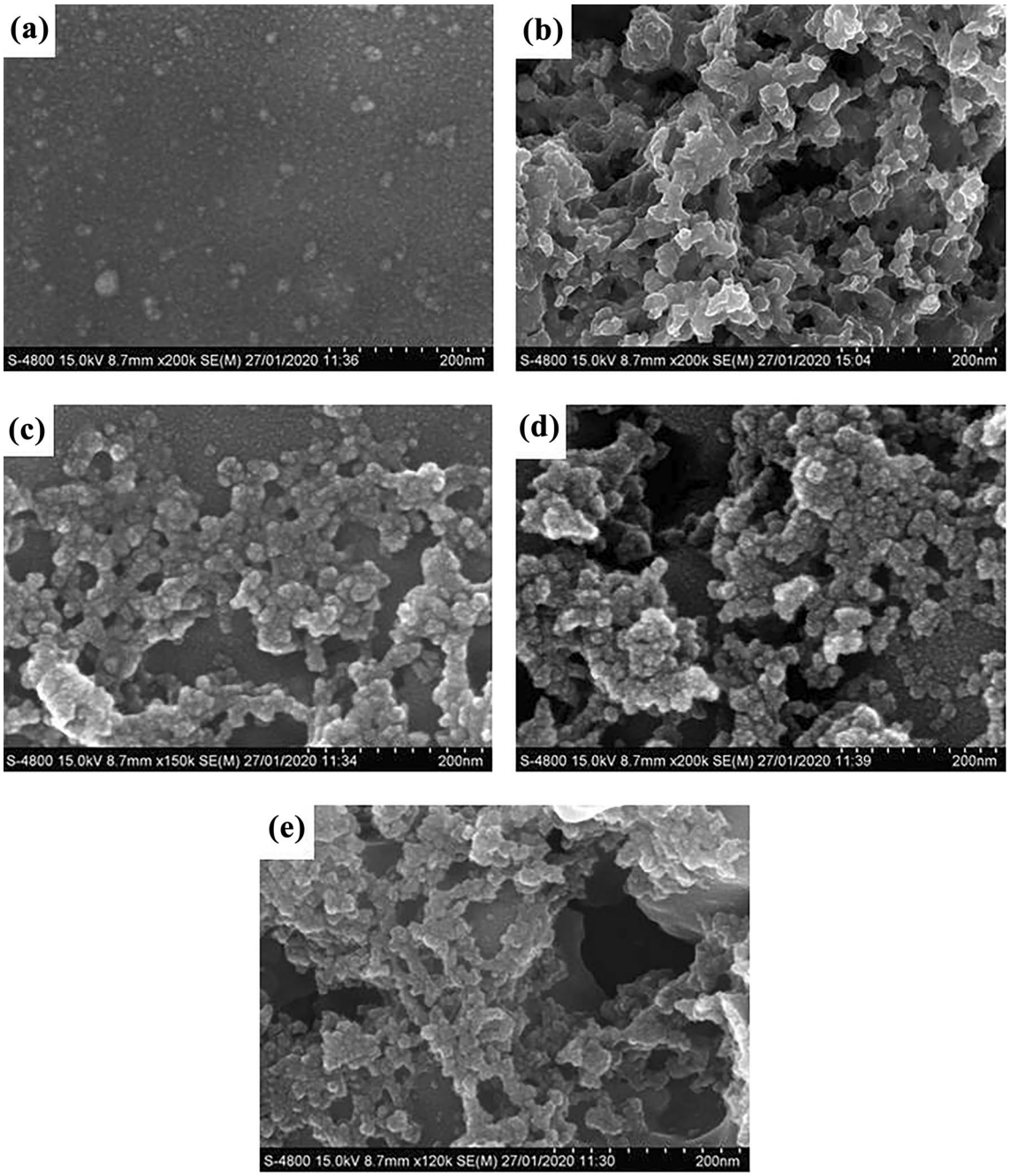

Fig. 3 FESEM images of RuO_2 films spray-deposited with various precursor solution concentrations **a** 12.5 mM, **b** 25 mM, **c** 37.5 mM, **d** 50 mM, and **e** 62.5 mM, respectively

RuO_2. In the present work, no other phases indicating the formation of pure RuO_2 films were detected.

The lattice parameters '*a*' and '*c*' were determined using a standard relation given elsewhere [42]. The lattice parameters for tetragonal RuO_2 are $a = b = 4.5220$ Å and $c = 3.1522$ Å, which are in good agreement with the standard values $a = b = 4.4930$ Å and $c = 3.1063$ Å [JCPDS Card No. 88-0322]. Table 1 shows structural data for RuO_2 films. It is observed that, by changing the concentration of the precursor solution, the lattice parameters do not change.

Crystallite size was determined using the Debye–Scherrer equation [43]. The width of the diffraction peaks increases with the concentration of the precursor solution, which clearly indicates a decrease in the crystallite size. The average crystallite size for the standard (110) plane was determined and found to decrease from 25 to 12 nm as the

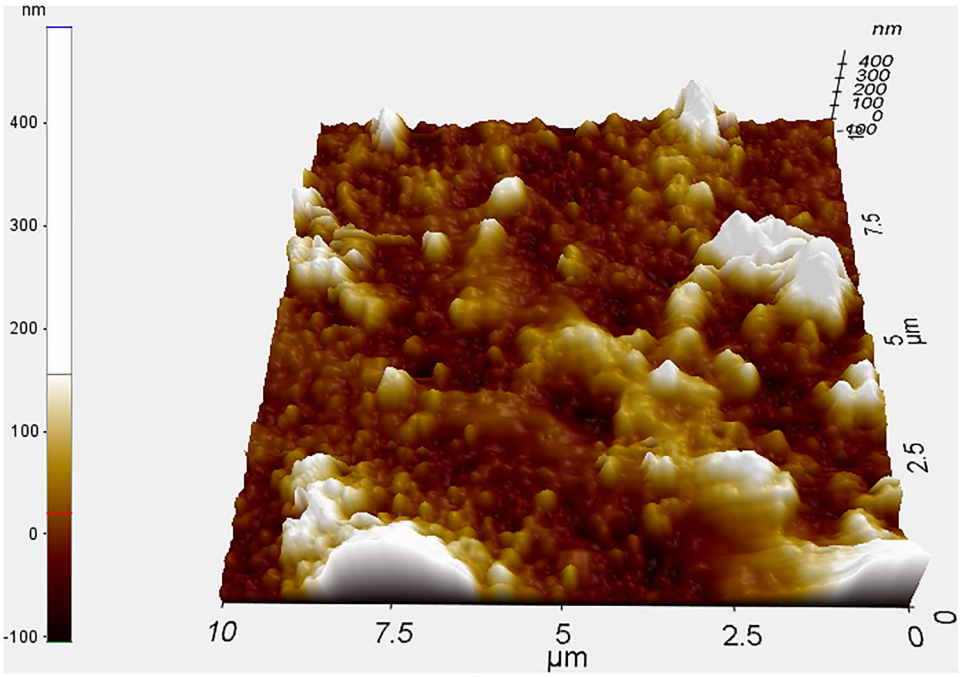

Fig. 4 AFM image of RuO_2 film spray-deposited with precursor solution concentration of 50 mM

precursor solution concentration increased from 12.5 to 62.5 mM. This behavior can be attributed to an increase in the film thickness of RuO_2 with an increase in the concentration of the precursor solution, resulting in improved order and reduced local states/defects [44]. Kannan and Sundararajan [45] reported 6–25 nm crystallite sizes for biosynthesis processed RuO_2 nanoparticles. Table 1 displays crystallite sizes for spray-deposited RuO_2 films.

3.3 FESEM

FESEM images of spray-deposited rutile RuO_2 films with various precursor solution concentrations are presented in Fig. 3a–e. RuO_2 films showed good crystalline particle structure. The surface morphology of RuO_2 films is modified by varying precursor solution concentrations. For RuO_2 films spray-deposited with a precursor solution concentration of 12.5 mM, the particles are more dense and agglomerated (Fig. 3a). With a rise in precursor solution concentration to 25 mM, RuO_2 film shows porous morphology and larger particles formed by controlled agglomeration of smaller particles (Fig. 3b). The porosity of spray-deposited RuO_2 films enhanced with an increase in the precursor solution concentration above 37.5 mM (Fig. 3c–e). Yang and colleagues [46] have reported such porous morphology for hydrothermally prepared RuO_2/RGOH and Lenar et al. [47] obtained

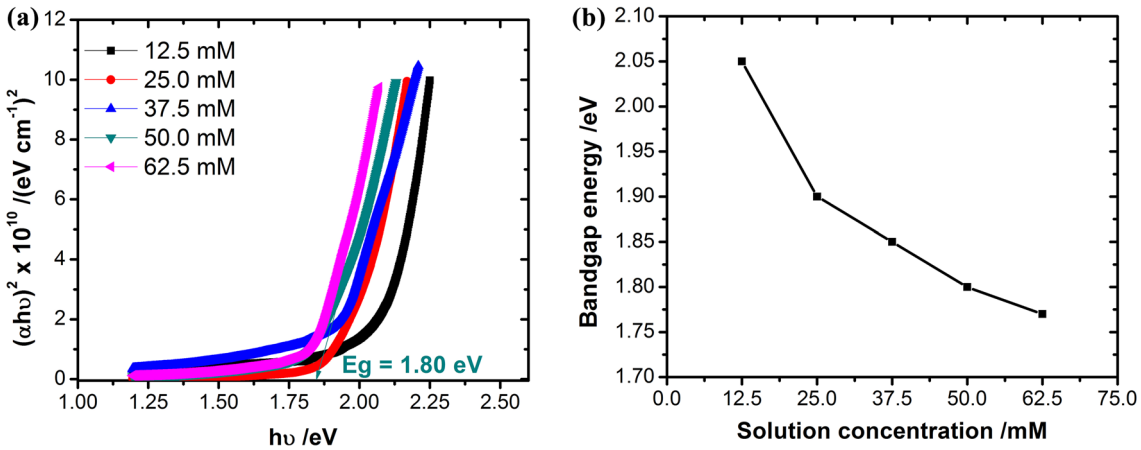

Fig. 5 **a** Variation of $(\alpha h\nu)^2$ as a function of $h\nu$ used for determination optical bandgap and **b** variation of bandgap energy with precursor solution concentration for RuO_2 films

Table 2 Optical and electrical properties of RuO_2 films spray-deposited with various precursor solution concentrations

Solution	Band gap	Electrical resistivity (Ω-cm)		Activation energy (eV)	
Conc. (mM)	(eV)	300 K ($\times 10^4$)	500 K ($\times 10^2$)	LT	HT
12.5	2.05	0.99	9.62	0.054	0.061
25.0	1.90	0.57	6.35	0.054	0.044
37.5	1.85	0.32	4.19	0.046	0.043
50.0	1.80	0.12	1.83	0.054	0.048
62.5	1.77	0.20	2.91	0.055	0.033

LT low temperature, *HT* high temperature

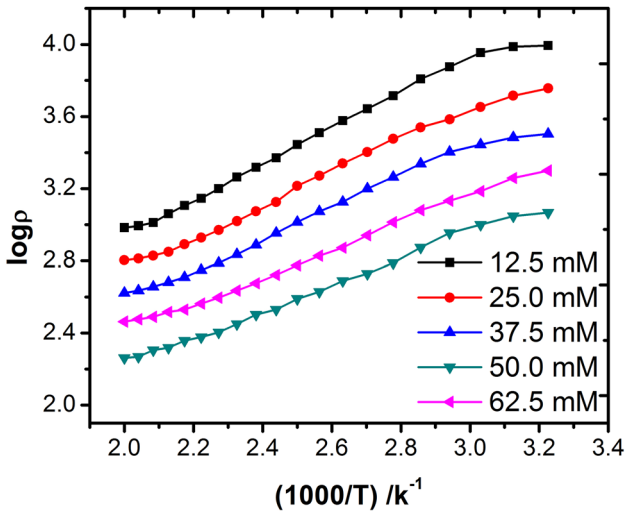

Fig. 6 Plot of log (ρ) versus 1000/T for RuO_2 films spray-deposited with various precursor solution concentrations

similar morphologies for RuO_2 nanoparticles. Indicatively, this porous morphology is useful in solar cells and energy storage devices.

3.4 AFM

Figure 4 shows the 3D surface topography of a 10×10 μm^2 area of a spray-deposited RuO_2 film with a precursor solution concentration of 50 mM. The surface topography clearly shows the complete coverage of the substrate surface distributed by interconnected grains. Aggregation of particles is evident from the AFM images, which illustrate the crystalline nature of the RuO_2 films. The observed surface roughness of the sample is ~ 100 nm. Surface morphology by FESEM and surface topography by AFM matched well for RuO_2 films. Ingole et al. [48] reported similar surface topography for spray-deposited nanoporous RuO_2 electrodes.

3.5 Optical

A useful tool for understanding the optical properties of nanostructured materials is UV–visible spectroscopy. The optical properties of RuO_2 depend on the synthesis method, experimental conditions, dopants and their concentration, and surface morphology [44]. UV–visible absorption spectra in the 350–1050 nm wavelength range are used to investigate the bandgap of spray-deposited RuO_2 films with various precursor solution concentrations. Absorption spectra showed a strong absorption band around 605 nm (12.5 mM), 653 nm (25 mM), 670 nm (37.5 mM), 688 nm (50 mM), and 700 nm (62.5 mM). The absorption variation is dominated by the precursor solution concentration and the absorption edge shifts toward longer wavelengths due to the Burstein-Moss shift [49].

Plots of $(\alpha h\nu)^2$ versus hν were plotted to determine the bandgap of RuO_2 films, as illustrated in Fig. 5a. Straight lines in the high-energy region specify direct allowed optical transitions. The bandgap of spray-deposited RuO_2 films was found from the absorption data using the well-known Tauc's law [50]. The bandgap was found by extrapolating the linear portion of the $(\alpha h\nu)^2$ versus hν plot along the energy axis at $\alpha = 0$. Figure 5b shows that the direct bandgap decreases from 2.05 to 1.77 eV with an increase in the concentration of the precursor solution. Table 2 shows the bandgap energies of RuO_2 films spray-deposited with various precursor solution concentrations. These values are close to the threshold bandgap of 1.8 eV obtained for RuO_2 single crystal [51]. The bandgap values obtained in the present work are close to 1.87 eV obtained by El-Tantawy et al. [52] for sol–gel prepared RuO_2, and 2.2 eV obtained by Patake and Lokhande [50] for chemically prepared RuO_2.

3.6 Electrical

Electrical characterization of spray-deposited RuO_2 films with various precursor solution concentrations was performed by the DC two-point probe method. The room temperature and high temperature electrical resistivities of the RuO_2 films are given in Table 2. A high electrical resistivity (0.99×10^4 Ω-cm) at room temperature is observed for RuO_2 film spray-deposited with 12.5 mM. As the precursor solution concentration increases upto 50 mM, the resistivity reaches a low value (0.12×10^4 Ω-cm) and then increases again to 0.20×10^4 Ω-cm for an increase in the precursor solution concentration to 62.5 mM. This may be due to the increase in film thickness of RuO_2 associated with the increase in precursor solution concentration [40]. To estimate the activation energy (*Ea*), the variation of film resistivity versus temperature from 300 to 500 K was recorded. Figure 6 depicts the plot of logρ against 1000/T for RuO_2 films. The electrical resistivity of RuO_2 films reduced with

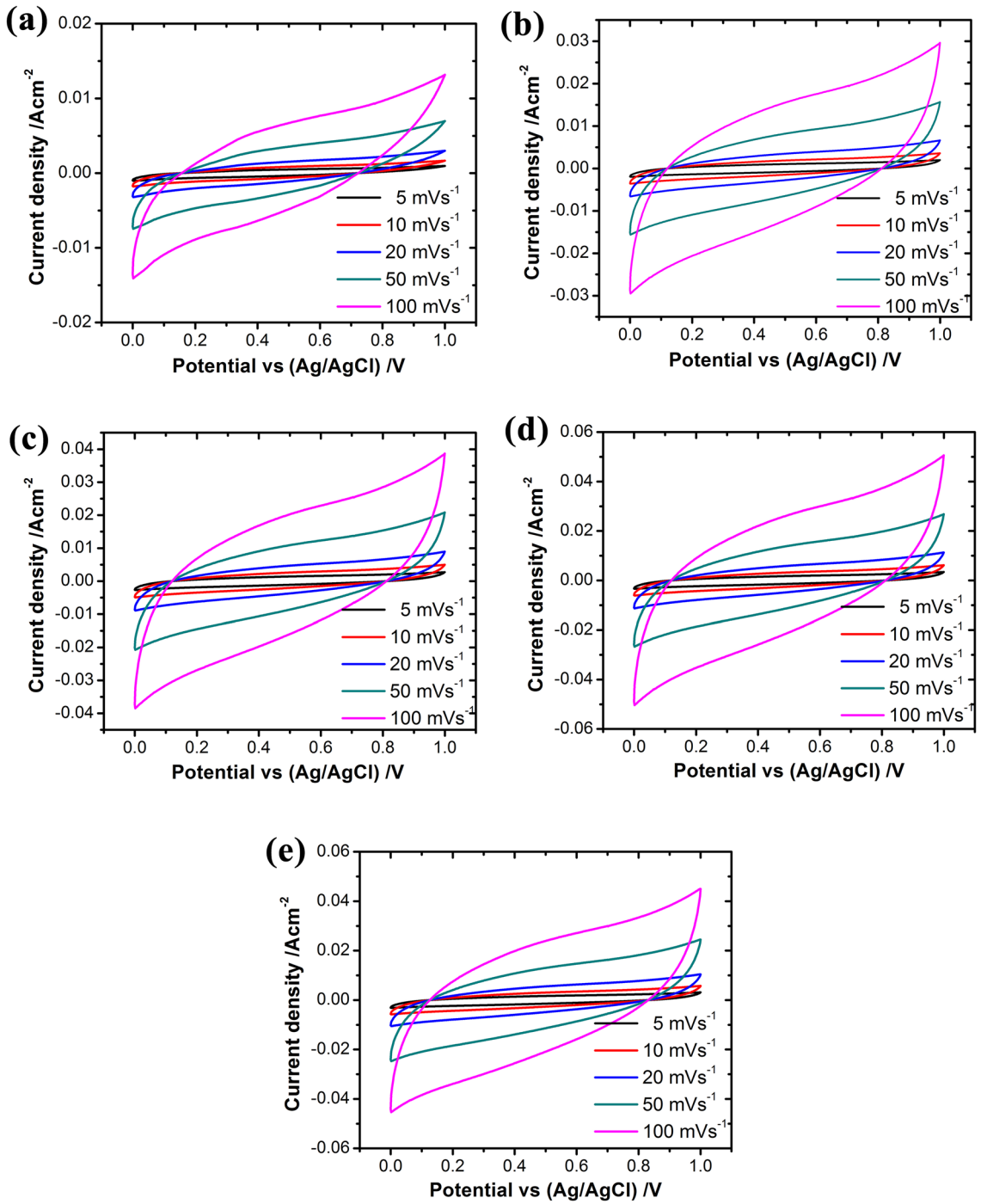

Fig. 7 CV Plots at scan rates of 5–100 mVs^{-1} for RuO_2 films prepared by spray pyrolysis with various precursor solution concentrations **a** 12.5 mM, **b** 25 mM, **c** 37.5 mM, **d** 50 mM, and **e** 62.5 mM; respectively

an increase in temperature, suggesting semiconducting behavior. The resistivity variance of RuO_2 films is approximated by the Arrhenius equation [53]. The activation energies were 0.046–0.055 eV and 0.033–0.061 eV in low temperature and high temperature regions, respectively. These activation energies are in accordance with values estimated from the work of Ribera et al. [54].

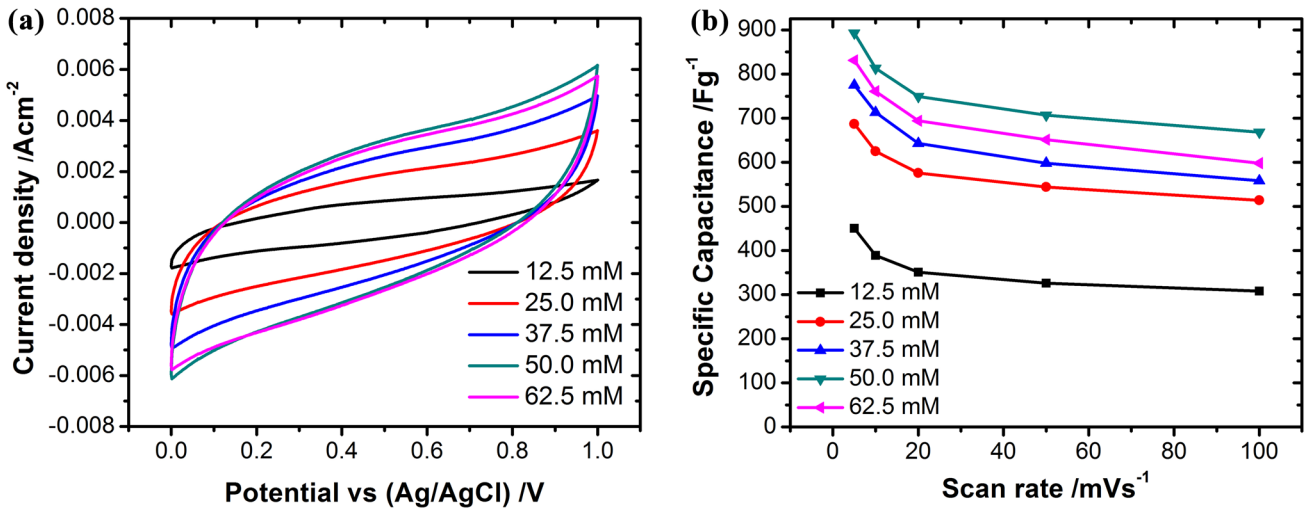

Fig. 8 **a** CV plots at scan rate of 10 mVs^{-1} and **b** variation of specific capacitance with scan rate for RuO_2 films prepared by spray pyrolysis with various precursor solution concentrations

Table 3 Specific capacitance at different scan rates from CV for RuO_2 films spray-deposited with various precursor solution concentrations

Solution Conc. (mM) →	12.5	25.0	37.5	50.0	62.5
Scan rate (mVs^{-1})↓	Specific capacitance from CV (Fg^{-1})				
5	450	687	775	893	831
10	389	625	713	813	761
20	351	576	643	749	694
50	326	544	598	707	651
100	308	514	558	668	598

3.7 Electrochemical

To investigate the potential applications, spray-deposited RuO_2 films with various precursor solution concentrations were fabricated into supercapacitor electrodes and evaluated using CV, GCD, and EIS, respectively.

3.7.1 CV

Figure 7a–e shows the CV plots in a wide potential range from 0.0 to 1.0 V (Ag/AgCl) in 0.5 M H_2SO_4 electrolyte at scan rates of 5–100 mVs^{-1} for RuO_2 films. All of the CV curves are slanted at low scan rates because the high electrical resistivity of RuO_2 contributes significantly to the total equivalent series resistance, lacking identifiable redox peaks and curves deviates from the ideal rectangle form. All of the RuO_2 electrodes showed much larger integrated areas, indicating excellent electrochemical performance. Figure 8a displays CV plots in 0.5 M H_2SO_4 electrolyte at 10 mVs^{-1} scan rate of RuO_2 films spray-deposited with various precursor solution concentrations. It is perceived that as the precursor solution concentration increases from 12.5 to 50 mM, the integrated area under the curve increases, which is attributed to the enhanced electrical conductivity [55]. At a 62.5 mM precursor solution concentration, the integrated area under the curve slightly decreases. The integrated areas under the CV curves were used to obtain the specific capacitance of RuO_2 using the equation given elsewhere [56]. Table 3 shows the specific capacitances (Csp) obtained from CV for RuO_2 films spray-deposited with various precursor solution concentrations. Figure 8b shows the variation of Csp with scan rate for RuO_2 films. From the graph, the Csp for RuO_2 film prepared with 50 mM falls from 893 to 668 Fg^{-1}, as the scan rate is increased from 5 to 100 mVs^{-1}. This illustrates the voltammetric current dependency on the scan rate. As the scan rate increases from 5 to 100 mVs^{-1}, the specific capacitance decreases due to the presence of inner active sites that cannot fully sustain redox transitions at higher scan rates [57].

The specific capacitance at scan rate 5 mVs^{-1} of RuO_2 film spray-deposited with 12.5 mM precursor solution concentration is 450 Fg^{-1}, which increased with an increase in precursor solution concentration up to 50 mM (893 Fg^{-1}). Specific capacitance at scan rate 5 mVs^{-1} was decreased to 831 Fg^{-1} for RuO_2 film spray-deposited with 62.5 mM precursor solution concentration due to the decreased electrical conductivity of the RuO_2. Overall, high specific capacitance is due to the nanocrystalline feature and porous morphology of the RuO_2. The specific capacitance of 893 Fg^{-1} obtained in present work is better than 209 Fg^{-1} at 5 mVs^{-1} for RuO_2 nanoparticles [58] and is comparable to 650 Fg^{-1} reported by Patake and colleagues [27] for electrodeposited RuO_2

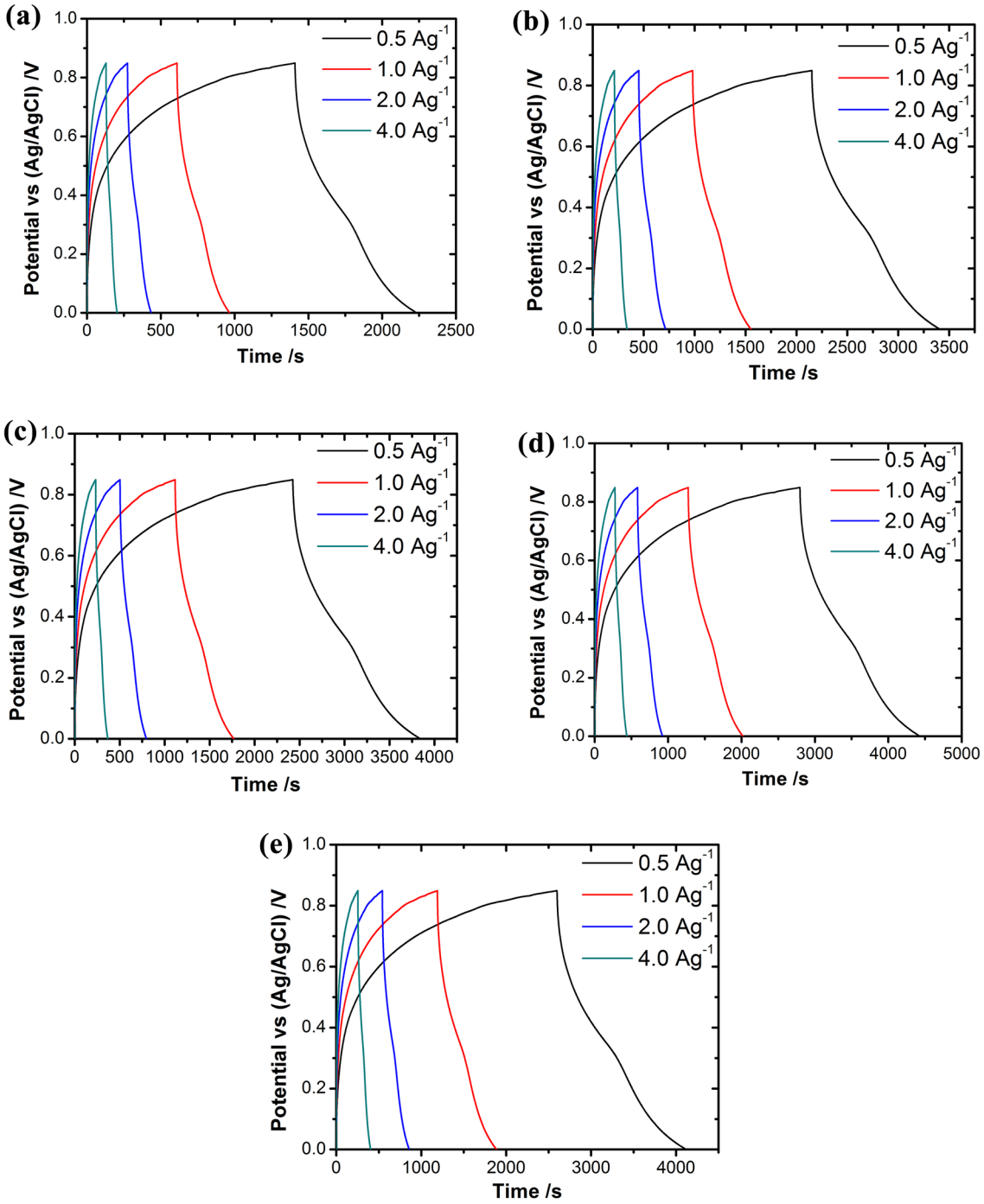

Fig. 9 GCD curves at different current densities for RuO_2 films prepared by spray pyrolysis with various precursor solution concentrations **a** 12.5 mM, **b** 25 mM, **c** 37.5 mM, **d** 50 mM, and **e** 62.5 mM; respectively

films and the 606 Fg^{-1} reported by Raja et al. [59] for RuO_2 particles.

3.7.2 GCD

Figure 9a–e shows GCD curves in 0.5 M H_2SO_4 electrolyte for RuO_2 films spray-deposited with various precursor solution concentrations with the potential range of 0.0–0.85 V (note that this is distinct from CV analysis). Using the

Table 4 Specific capacitances from GCD for RuO_2 films spray-deposited with various precursor solution concentrations

Solution Conc. (mM) →	12.5	25.0	37.5	50.0	62.5
Current density (Ag^{-1}) ↓	Specific capacitance from GCD (Fg^{-1})				
0.5	486	741	837	964	897
1	420	675	770	878	821
2	380	622	694	808	749
4	352	586	645	763	703

experimental data demonstrated in the GCD curve, the specific capacitance has been calculated from the relationship given elsewhere [26]. Table 4 shows the specific capacitances obtained from GCD curves. Accordingly, as the precursor solution concentration increases from 12.5 to 50 mM, the specific capacitance (at a current density 0.5 Ag^{-1}) increases from 486 to 964 Fg^{-1}. The increase in specific capacitance with increasing precursor solution concentration is due to improved microstructure and morphology (as observed from XRD and FESEM). The results acquired in this work (964 Fg^{-1} at 0.5 Ag^{-1} current density) are equivalent to or exceeding those mentioned in the literature for RuO_2 based systems, where the specific capacitance was reported to be around 200 Fg^{-1}, 276 Fg^{-1}, and 788 Fg^{-1} [29, 60, 61]. Table 5 summarizes the recent research works that

Table 5 The capacitive performance comparison of RuO_2 films in this work with various RuO_2 reported in some literatures

Order	Material	Electrolyte	Measurement Protocol	Max capacitance	Refs.
1	RuO_2 NNs/Ta/Cu	diluted H_2SO_4	GCD@50 mA cm^{-2}	580 Fg^{-1}	[12]
2	RuO_2	0.5 M H_2SO_4	CV@20 mVs^{-1}	650 Fg^{-1}	[27]
3	RuO_2	0.5 M H_2SO_4	CV@10 mVs^{-1}	788 F g^{-1}	[29]
4	RuO_2	1 M H_2SO_4	GCD@500 mAg^{-1}	860 Fg^{-1}	[30]
5	RuO_2	0.5 M H_2SO_4	CV@10 mVs^{-1}	162 Fg^{-1}	[32]
6	RuO_2	0.5 M H_2SO_4	CV@5 mVs^{-1}	551 Fg^{-1}	[36]
7	RuO_2	1 M KOH	CV@5 mVs^{-1}	787 Fg^{-1}	[48]
8	RuO_2	0.5 M H_2SO_4	CV@20 mVs^{-1}	50 Fg^{-1}	[50]
9	RuO_2	0.5 M H_2SO_4	CV@5 mVs^{-1}	209 Fg^{-1}	[58]
10	RuO_2	1 M H_2SO_4	GCD@0.1A g^{-1}	111 Fg^{-1}	[59]
11	RuO_2	1 M KOH	GCD@0.8A g^{-1}	200 Fg^{-1}	[60]
12	RuO_2	0.5 M H_2SO_4	GCD@13.33A g^{-1}	276 Fg^{-1}	[61]
13	RuO_2	0.5 M H_2SO_4	CV@2 mVs^{-1}	73 Fg^{-1}	[62]
14	This work	0.5 M H_2SO_4	CV@5 mVs^{-1}	893 Fg^{-1}	–
	This work	0.5 M H_2SO_4	GCD@0.5 Ag^{-1}	964 Fg^{-1}	–

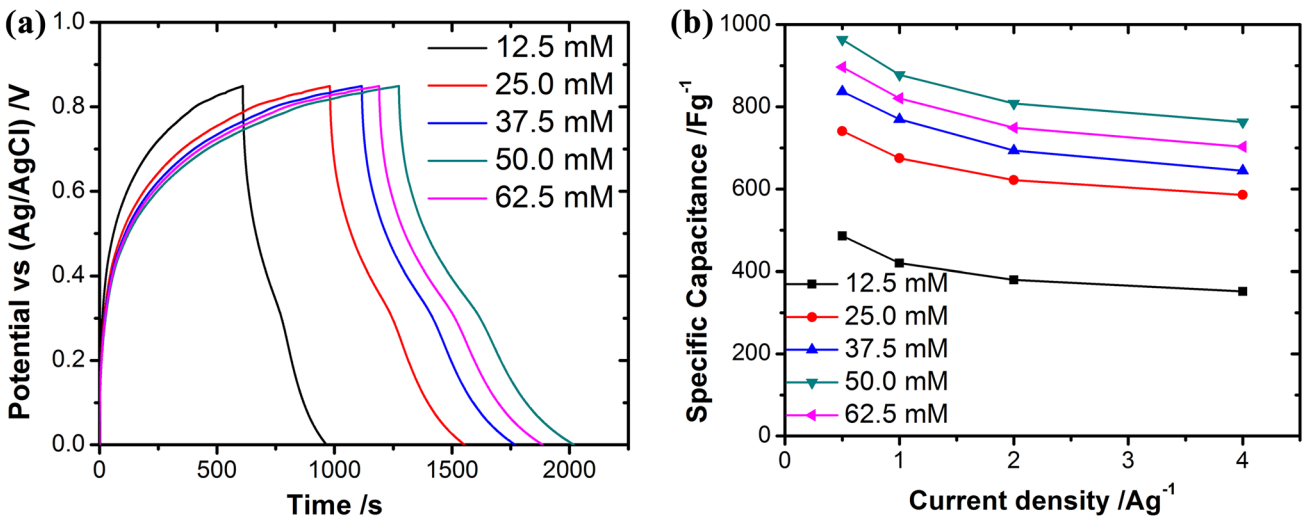

Fig. 10 **a** GCD curves at current density of 1Ag^{-1} and **b** plot of specific capacitance versus current density for RuO_2 electrodes prepared by spray pyrolysis with various solution concentrations

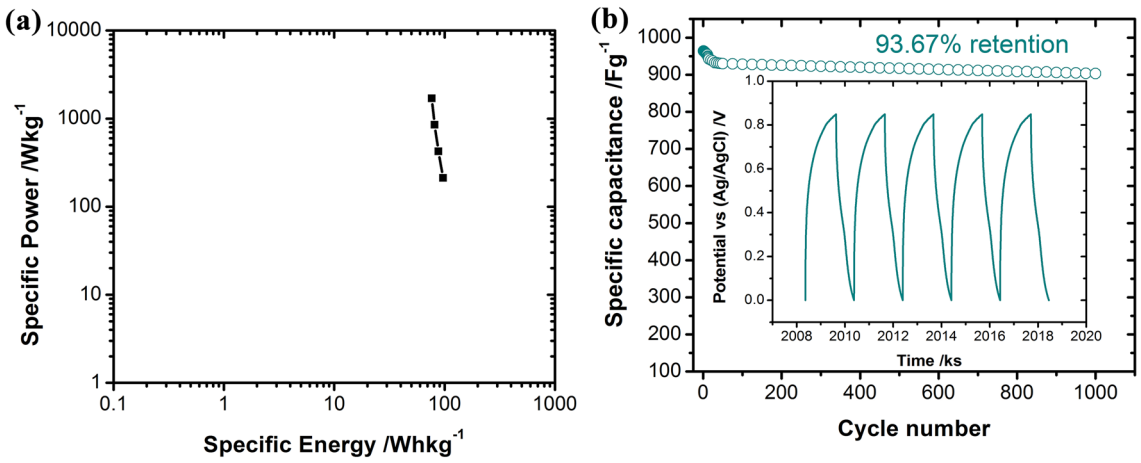

Fig. 11 **a** Ragone plot of RuO_2 electrode prepared with precursor solution concentration of 50 mM and **b** long-term cycling performance of the RuO_2 films spray-deposited with solution concentration of 50 mM and at the current density of $1Ag^{-1}$. The inset shows the charge–discharge curves of the last 5 cycles of the RuO_2 films

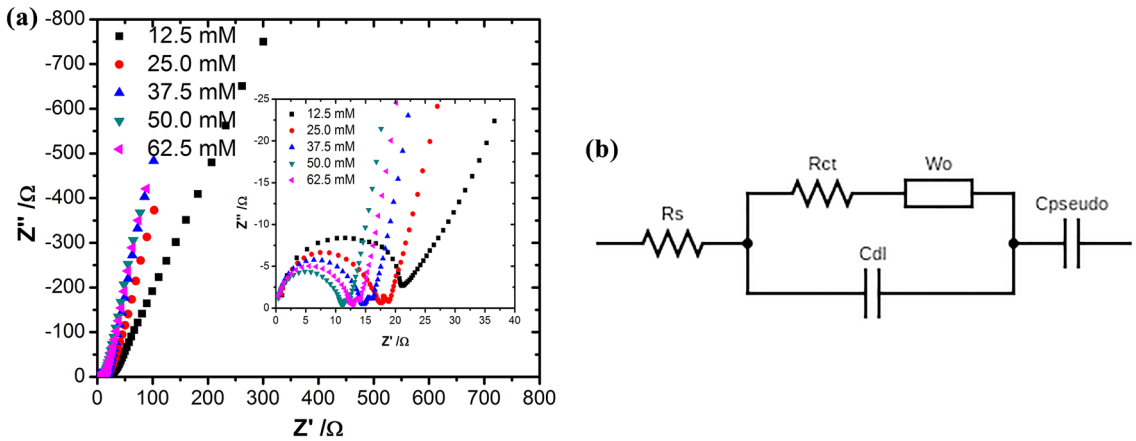

Fig. 12 Nyquist plot for RuO_2 film electrodes prepared by spray pyrolysis with various solution concentrations. (The inset is the enlarged Nyquist plots in high frequency region) and **b** equivalent circuit diagram proposed for analysis of the EIS data

were carried out in the literature for RuO_2 based systems, including different electrolytes employed.

Figure 10a displays the GCD curves at 1 Ag^{-1} current density for RuO_2 electrodes spray-deposited with various precursor solution concentrations. All the charge–discharge curves are linear and symmetric in the voltage range 0–0.85 V, indicating good electrochemical properties. Moreover, the potential-time relationship of GCD curves shows a nonlinear relationship, demonstrating a combination of EDLC and pseudocapacitance.

Figure 10b shows the plot of specific capacitance against current density for RuO_2 electrodes spray-deposited with various solution concentrations. As expected, the specific capacitance of RuO_2 electrodes decreased with the increase in current density. What should be stated is that at a large current density (4 Ag^{-1}), specific capacitance of RuO_2 electrodes prepared with 50 mM still remained at about 763 Fg^{-1}, while the specific capacitance of RuO_2 electrodes prepared with 12.5 mM precursor solution concentration reduced to only 352 Fg^{-1}. Such outcomes indicate that the RuO_2 electrodes prepared with a 50 mM precursor solution concentration show remarkable electrochemical performance.

Specific power and specific energy of device fabricated with RuO_2 electrodes have also been calculated using equations given elsewhere [26] and are shown as Ragone plot in Fig. 11a. The highest specific power and specific energy of RuO_2 electrodes prepared with 50 mM precursor solution concentration are 1701 Wkg^{-1} and 76.56 $Whkg^{-1}$ respectively, at $4Ag^{-1}$. These values are comparable to specific energy values of 3.57Wh kg^{-1} and specific power values of 151 Wkg^{-1} reported by Patil et al. [62] for chemically

Table 6 Nyquist data for RuO_2 films spray-deposited with various precursor solution concentrations

Solution Concentration (mM)	Rs (Ω)	Rct (Ωcm^2)
12.5	0.78	21.15
25.0	0.40	17.10
37.5	0.35	14.50
50.0	0.32	11.38
62.5	0.33	13.63

synthesized hydrous RuO_2. Overall, the electrochemical study makes the RuO_2 electrode prepared with a 50 mM precursor solution concentration as a great electrode for supercapacitor applications.

Another critical factor in evaluating the quality of supercapacitors is cycling stability. Figure 11b shows the long-term cycling performance at $1Ag^{-1}$ current density for 1000 cycles of RuO_2 electrode spray-deposited with a 50 mM precursor solution concentration. The capacitance retention remains as high as 93.67% after 1000 charging/discharging cycles. RuO_2 electrode does not experience substantial structural changes during charging/discharging processes, as shown by the charging-discharging curve of RuO_2 film in the last 5 cycles, which is depicted in the inset of Fig. 11b.

3.7.3 EIS

EIS is a very significant measure to assess the quality of supercapacitors. Figure 12a displays the impedance curves of the supercapacitors based on RuO_2 electrodes spray-deposited with various precursor solution concentrations, measured in a 0.5 M H_2SO_4 electrolyte solution. The inset is the enlarged Nyquist plots in high frequency region. The EIS data can be fitted by an equivalent circuit shown in Fig. 12b. The elements in the equivalent circuit are solution resistance (Rs), the charge-transfer resistance (Rct), the double-layer capacitance (Cdl), the Warburg diffusion element (Wo), and the pseudocapacitance element (Cpseudo). The horizontal axis intercepts in the high frequency region in the Nyquist plots for the supercapacitors based on RuO_2 electrodes spray-deposited with various precursor solution concentrations 12.5 mM, 25 mM, 37.5 mM, 50 mM, and 62.5 mM, are, respectively, 0.78, 0.40, 0.35, 0.32, and 0.33 Ω indicating that with the change in precursor solution concentration, the solution resistance (Rs) changes unnoticeably. The RuO_2 electrode deposited with a 50 mM precursor solution concentration had an upright slope in the low frequency region in synchrony with the CV graphs than RuO_2 electrodes deposited at other precursor solution concentrations, indicating that the RuO_2 electrode deposited with a 50 mM precursor solution concentration had a higher capacitive response and lower diffusion resistance toward the electrolyte ions on the electrode surface. The radius of the semicircle represents the charge transfer resistance (Rct) at the RuO_2 electrode/0.5 M H_2SO_4 electrolyte interface. The values of Rct are tabulated in Table 6. From Table 6 and Fig. 12a the RuO_2 electrode spray-deposited with a precursor solution concentration of 50 mM showed a minimum Rct demonstrating improved electronic and ionic conductivities [63].

4 Conclusion

The use of aqueous/organic mixtures improves the electrochemical performance of RuO_2 electrodes. Structural analysis indicated that the RuO_2 film was oriented along the (110) plane. The (110) peak intensity increased with the increasing concentration of the precursor solution. Surface morphology studies of RuO_2 electrodes have shown that it is possible to obtain a porous morphology by varying the precursor solution concentration. The direct allowed bandgap of the RuO_2 electrode decreases from 2.05 to 1.77 eV with precursor solution concentration from 12.5 to 62.5 mM. The electrical resistivity of the RuO_2 decreases with an increase in precursor solution concentration and is least 0.12×10^4 Ωcm at a precursor solution concentration of 50 mM. The RuO_2 electrode with a precursor solution concentration of 50 mM showed outstanding electrochemical performance with specific capacitance from CV of 893 Fg^{-1} at 5 mVs^{-1} scan rate, with a specific capacitance from GCD of 964 Fg^{-1} at 0.5 Ag^{-1}, retaining a specific capacity of 93.67% capacitance after 1000 cycles, specific energy of 76.56 $Whkg^{-1}$, and specific power of 1701 Wkg^{-1} than others. Findings from this study will help in the fabrication of RuO_2 film-based supercapacitors with good energy retention and high specific energy and push forward the progress of supercapacitors into practical applications.

Author contribution All authors contributed to the study conception and design. Material preparation, data collection and analysis were performed by all authors. The first draft of the manuscript was written by Chandrashekhar R., and Dr Abhijit Yadav commented on previous versions of the manuscript. All authors read and approved the final manuscript.

Funding There are no financial or non-financial interests.

Data availability It is hereby assured that materials described in the manuscript, including all relevant raw data, will be freely available to any researcher wishing to use them for non-commercial purposes, without breaching participant confidentiality.

Declarations

Conflict of interest There is no conflict to declare.

Human and animal participation This article does not contain any studies with human or animal subjects.

References

1. Zhai Z, Zhang L, Tianmin Du, Ren B, Yuelong Xu, Wang S, Miao J, Liu Z (2022) A review of carbon materials for supercapacitors. Mater Des 221:111017
2. Gomez Vidales A, Sridhar D, Meunier JL, Omanovic S (2020) Nickel oxide on directly grown carbon nanofibers for energy storage applications. J Appl Electrochem 50:1217–1229
3. Chakraborty S, Simon R, Antonia TZR, Anoop V, Mary NL (2022) Microwave-assisted synthesis of ZnO decorated acid functionalized carbon nanotubes with improved specific capacitance. J Appl Electrochem 52:103–114
4. Abas A, Omer AA, Wei I, Lu Q (2022) Efficient synthesis of enwrapped CuO@rGO nanowire arrays to improve supercapacitor electrode performance. J Appl Electrochem 52:813–820
5. Kate RS, Pathan HM, Kalubarme R, Kale BB, Deokate RJ (2022) Spray pyrolysis: approaches for nanostructured metal oxide films in energy storage application. J Energy Storage 54:105387
6. Wang G, Kuangliang Xu, Yan Z, Wang G, Xiang M, Zhihua Xu (2022) Hierarchical MnO_2/hollow carbon spheres composites for asymmetric supercapacitors with enhanced performance. J Appl Electrochem 52:963–978
7. Conway BE (1999) The electrochemical behavior of ruthenium oxide (RuO2) as a material for electrochemical capacitors. In: Electrochemical Supercapacitors. Springer, Boston, MA. https://doi.org/10.1007/978-1-4757-3058-6_11
8. Filimonenkov IS, Urvanov SA, Kazennov NV, Tarelkin SA, Tsirlina GA, Mordkovich VZ (2022) Carbon nanotube cloth as a promising electrode material for flexible aqueous supercapacitors. J Appl Electrochem 52:487–498
9. Navajsharif SS, Shivaji BU, Vikas JM, Jasmin SS, Vaibhav CL, Supareak P, Chandrakant DL, Pongsakorn K (2022) Novel electrodes for supercapacitor: Conducting polymers, metal oxides, chalcogenides, carbides, nitrides, MXenes, and their composites with graphene. J Alloys Compd. 893:161998
10. Shown I, Ganguly A, Chen L-C, Chen K-H (2015) Conducting polymer-based flexible supercapacitor. Energy Sci Eng 3:2–26
11. Zhang B-B, Hao H, Zhang F-Y, Wang B, Xue J, Jiao L-Y, Li Z (2020) SubPc-Br/NiMoO4 composite as a high-performance supercapacitor electrode materials. J Appl Electrochem 50:1007–1018
12. Cho S, Kim J, Han J, Shin G, Park S, Yeon S, Jana A, Kim H, Im H (2022) Self-assembled RuO_2 nanoneedles on Ta/Cu foil for a robust and high-performance supercapacitor electrode. Surf Interfaces 31:102069
13. Yadav AA, Jadhav SN, Chougule DM, Patil PD, Chavan UJ, Kolekar YD (2016) Spray-deposited Hausmannite Mn_3O_4 thin films using aqueous/organic solvent mixture for supercapacitor applications. Electrochim Acta 206:134–142
14. Rohan BA, Hojae L, Ki HL, Hyeonhoo L, Ganesh KV, Young-Beom K, Tae HH (2022) Ultrafast flashlight sintered mesoporous NiO nanosheets for stable asymmetric supercapacitors. Chem. Eng. J. 436:135041
15. Kate RS, Khalate SA, Deokate RJ (2018) Overview of nanostructured metal oxides and pure nickel oxide (NiO) electrodes for supercapacitors: a review. J Alloys Compd 734:89–111
16. Deokate RJ, Kate R, Shinde NM, Mane RS (2021) Energy storage potential of sprayed α-MoO_3 thin films. New J Chem 45:582–589
17. Yadav AA (2021) Physical and electrochemical properties of spray-deposited Co_3O_4 thin films. Phase Transit 94(10):691–704
18. Deokate RJ, Kalubarme RS, Park C-J, Lokhande CD (2017) Simple synthesis of $NiCo_2O_4$ thin films using spray pyrolysis for electrochemical supercapacitor application: a novel approach. Electrochim Acta 224:378–385
19. Yadav AA, Deshmukh TB, Deshmukh RV, Patil DD, Chavan UJ (2016) Electrochemical supercapacitive performance of Hematite α-Fe_2O_3 thin films prepared by spray pyrolysis from non-aqueous medium. Thin Solid Films 616:351–358
20. Yadav AA (2016) Preparation and electrochemical properties of spray-deposited α-Fe_2O_3 from nonaqueous medium for supercapacitor applications. J Mater Sci Mater Electron 27:12876–12883
21. Balamuralitharan B, Cho IH, Bak JS, Kim HJ (2018) V_2O_5 nanorod electrode material for enhanced electrochemical properties by a facile hydrothermal method for supercapacitor applications. New J Chem 42:11862–11868
22. Ingole RS, Kondawar SB, Lokhande BJ (2016) Substrate dependent morphological and electrochemical properties of V_2O_5 thin films prepared by spray pyrolysis. J Mater Sci Mater Electron 28(3):2385–2391
23. Ingole RS, Lokhande BJ (2016) Electrochemical properties of dip-coated vanadium pentaoxide thin films. Bull Mater Sci 39:1603–1608
24. Zhang Q, Dawei Gu, Li H, Ze Xu, Sun H, Li J, Wang L, Shen L (2021) Energy release from RuO_2//RuO_2 supercapacitors under dynamic discharge conditions. Electrochim Acta 367:137455
25. Fugare BY, Lokhande BJ (2017) Study on structural, morphological, electrochemical and corrosion properties of mesoporous RuO_2 thin films prepared by ultrasonic spray pyrolysis for supercapacitor electrode application. Mater Sci Semicond Process 71:121–127
26. Majumdar D, Maiyalagan T, Jiang Z (2019) Recent progress in ruthenium oxide-based composites for supercapacitor applications. ChemElectroChem 6:4343–4372
27. Patake VD, Lokhande CD, Joo OS (2009) Electrodeposited ruthenium oxide thin films for supercapacitor: Effect of surface treatments. Appl Surf Sci 255:4192–4196
28. Warren R, Sammoura F, Tounsi F, Sanghadasa M, Lin L (2015) Highly active ruthenium oxide coating via ALD and electrochemical activation in supercapacitor applications. J Mater Chem A 3:15568–15575
29. Park BO, Lokhande CD, Park HS, Jung KD, Joo OS (2004) Performance of supercapacitor with electrodeposited ruthenium oxide film electrodes-effect of film thickness. J Power Sources 134:148–152
30. Zhang J, Ma J, Zhang LL, Guo P, Jiang J, Zhao XS (2010) Template synthesis of tubular ruthenium oxides for supercapacitor applications. J Phys Chem C 114:13608–13613
31. Yoon YS, Cho WI, Lim JH, Choi DJ (2001) Solid-state thin-film supercapacitor with ruthenium oxide and solid electrolyte thin films. J Power Sources 101:126–129
32. Deshmukh PR, Pusawale SN, Jagadale AD, Lokhande CD (2012) Supercapacitive performance of hydrous ruthenium oxide (RuO_2·nH_2O) thin films deposited by SILAR method. J Mater Sci 47:1546–1553
33. Luu TL, Ye KJ, Yong YJ (2017) Facile chemical bath deposition to fabricate RuO_2 electrodes for electrochemical chlorine evolution. Desalination Water Treat 99:204–210
34. Patil PS, Ennaoui EA, Lokhande CD, Müller M, Giersig M, Diesner K, Tributsch H (1997) Characterization of ultrasonic spray pyrolysed ruthenium oxide thin films. Thin Solid Films 310:57–62
35. Košević M, Stopic S, Bulan A, Kintrup J, Weber R, Stevanović J, Panić V, Friedrich B (2017) A continuous process for the ultrasonic spray pyrolysis synthesis of RuO_2/TiO_2 particles and their application as a coating of activated titanium anode. Adv Powder Technol 28:43–49
36. Gujar TP, Shinde VR, Lokhande CD, Kim WY, Jung KD, Joo OS (2007) Spray-deposited amorphous RuO_2 for an effective use in electrochemical supercapacitor. Electrochem Commun 9:504–510

37. Barote MA, Kamble SS, Yadav AA, Suryavanshi RV, Deshmukh LP, Masumdar EU (2012) Thickness dependence of $Cd_{0.825}Pb_{0.175}S$ thin film properties. Mater Lett 78:113–115
38. Dhole IA, Navale YH, Pawar CS, Navale ST, Patil VB (2018) Physicochemical and supercapacitive properties of electroplated nickel oxide electrode: effect of solution molarity. J Mater Sci Mater Electron 29:5675–5687
39. JCPDS card No. 88-0322
40. Mahmoud SA, Akl AA, Kamal H, Abdel-Hady K (2002) Opto-structural, electrical and electrochromic properties of crystalline nickel oxide thin films prepared by spray pyrolysis. Physica B 311:366–375
41. Kim YL, Choi HA, Lee NS, Son B, Kim HJ, Baik JM, Lee Y, Lee C, Kim MH (2015) RuO_2-ReO_3 composite nanofibers for efficient electrocatalytic responses. Phys Chem Chem Phys 17:7435–7442
42. Cullity BD (1956) Elements of X-ray diffraction. Addison Wesley Publishing Company, Boston
43. Scherrer P (1918) Nachrichten von der Gesellschaft der Wissenschaften zu Göttingen, Mathematisch-Physikalische Klasse. vol. 2, 98–100
44. Munawar T, Rehman MN, Nadeem MS, Mukhtar F, Manzoor S, Ashiq MN, Iqbal F (2021) Facile synthesis of Cr–Co co-doped CdO nanowires for photocatalytic, antimicrobial, and supercapacitor applications. J Alloys Compd 885:160885
45. Kannan SK, Sundrarajan M (2015) Green synthesis of ruthenium oxide nanoparticles: Characterization and its antibacterial activity. Adv Powder Technol 26:1505–1511
46. Yang Y, Liang Y, Zhang Y, Zhang Z, Li Z, Zhongai Hu (2015) Three-dimensional graphene hydrogel supported ultrafine RuO_2 nanoparticles for supercapacitor electrodes. New J Chem 39:4035–4040
47. Lenar N, Paczosa-Bator B, Piech R (2019) Ruthenium dioxide nanoparticles as a high-capacity transducer in solid-contact polymer membrane-based pH-selective electrodes. Microchim Acta 186:777
48. Ingole RS, Fugare BY, Lokhande BJ (2017) Ultrahigh specific capacitance of spray-deposited nanoporous interconnected ruthenium oxide electrode fabric for supercharged capacitor. J Mater Sci Mater Electron 28:16374–16383
49. Babar AR, Shinde SS, Moholkar AV, Bhosale CH, Kim JH, Rajpure KY (2011) Sensing properties of sprayed antimony doped tin oxide thin films: Solution molarity. J Alloys Compd 509:3108–3115
50. Patake VD, Lokhande CD (2008) Chemical synthesis of nanoporous ruthenium oxide (RuO_2) thin films for supercapacitor application. Appl Surf Sci 254:2820–2824
51. Belkind A, Orban Z, Vossen JL, Woollam JA (1992) Optical properties of RuO_2 films deposited by reactive sputtering. Thin Solid Films 207:242–247
52. El-Tantawy F, Al-Ghamdi AA, Al-Ghamdi AA, Al-Turki YA, Alshahrie A, Al-Hazmi F, Al-Hartomy OA (2017) Optical properties of nanostructured ruthenium dioxide thin films via sol-gel approach. J Mater Sci Mater Electron 28:52–59
53. Yadav AA, Barote MA, Masumdar EU (2010) Studies on cadmium selenide (CdSe) thin films deposited by spray pyrolysis. Mater Chem Phys 121:53–57
54. Ribera RC, van de Kruijs RWE, Yakshin AE, Bijkerk F (2015) Determination of oxygen diffusion kinetics during thin film ruthenium oxidation. J Appl Phys 118:055303
55. Kim M, Hwang Y, Min K, Kim J (2013) Concentration dependence of graphene oxide/nanoneedle manganese oxide composites reduced by hydrazine hydrate for electrochemical supercapacitor. Phys Chem Chem Phys 15:15602–15611
56. Yadav AA, Chavan UJ (2017) Electrochemical supercapacitive performance of spray-deposited $NiSnO_3$ thin films. Thin Solid Films 634:33–39
57. More PD, Jadhav PR, Ghanwat AA, Dhole IA, Navale YH, Patil VB (2017) Spray synthesized hydrophobic α-Fe_2O_3 thin film electrodes for supercapacitor application. J Mater Sci Mater Electron 28:17839–17848
58. Nisha B, Vidyalakshmi Y, Razack SA (2020) Enhanced formation of ruthenium oxide nanoparticles through green synthesis for highly efficient supercapacitor applications. Adv Powder Technol 31:1001–1006
59. Raja A, Son N, Swaminathan M, Kang M (2022) Electrochemical behavior of heteroatom doped on reduced graphene oxide with RuO_2 for HER, OER, and supercapacitor applications. J Taiwan Inst Chem Eng 138:104471
60. Sarkar S, Mukherjee D, Harini R, Nagaraju G (2022) Ionic liquid-assisted synthesis of tri-functional ruthenium oxide nanoplatelets for electrochemical energy applications. J Mater Sci 57:7680–7693
61. Mondal SK, Munichandraiah N (2008) Anodic deposition of porous RuO_2 on stainless steel for supercapacitor studies at high current densities. J Power Sources 175:657–663
62. Patil UM, Kulkarni SB, Jamadade VS, Lokhande CD (2011) Chemically synthesized hydrous RuO_2 thin films for supercapacitor application. J Alloys Comp 509:1677–1682
63. Zhang C, Zhu X, Wang Z, Sun P, Ren Y, Zhu J, Zhu J, Xiao D (2014) Facile synthesis and strongly microstructure-dependent electrochemical properties of graphene/manganese dioxide composites for supercapacitors. Nanoscale Res Lett 9:490

Publisher's Note Springer Nature remains neutral with regard to jurisdictional claims in published maps and institutional affiliations.

Springer Nature or its licensor (e.g. a society or other partner) holds exclusive rights to this article under a publishing agreement with the author(s) or other rightsholder(s); author self-archiving of the accepted manuscript version of this article is solely governed by the terms of such publishing agreement and applicable law.

Authors and Affiliations

Chandrashekhar R. Chikkegowda[1] · Abhijit A. Yadav[1]

✉ Abhijit A. Yadav
aay_physics@yahoo.co.in

[1] Thin Film Physics Laboratory, Department of Physics, Electronics and Photonics, Rajarshi Shahu Mahavidyalaya (Autonomous), Latur, Maharashtra 413512, India